

# Solvent-free Synthesis and Characterization of MnO<sub>2</sub> Nanostructures and Investigation of Optical Properties

Sedyghe Akbari<sup>1\*</sup>, Mohammad Mehdi Foroughi<sup>1</sup> and Mehdi Ranjbar<sup>2</sup>

<sup>1</sup>Department of Chemistry, Kerman Branch, Islamic Azad University, Kerman, Iran

<sup>2</sup>Pharmaceutics Research Center, Kerman University of Medical Sciences, Kerman, Iran

## Abstract

This paper reports on a novel processing route for producing MnO<sub>2</sub> nanocomposites by solid-state thermal decomposition of manganese (II) acetylacetonate nanostructures from manganese(II) acetylacetonate powder as starting reagents, in the temperature 200°C for 4 h.

Finally, the efficiency of MnO<sub>2</sub> nanostructures as an optical investigation using PL spectrum has been evaluated. The as-synthesized nanoproducts were characterized by X-ray diffraction (XRD), scanning electron microscopy (SEM), transmission electron microscopy (TEM), photoluminescence (PL) spectroscopy and Infrared Spectroscopy (IR). The sublimation process of the Mn(OAc)<sub>2</sub> powder was carried out within the range of 200°C, 210°C, 220°C, and 230°C. MnO<sub>2</sub> nanocomposites showed strong photoluminescence excited at 383 nm which showed this structures exhibited optical properties behavior at room temperature. In this study simulation calculations were done by the Taguchi technique for systematic optimizing of the parameter on the size distribution of the MnO<sub>2</sub> nanocomposites.

**Keywords:** Nanoparticles; Oxidation; MnO<sub>2</sub>; Thermal decomposition

## Introduction

MnO<sub>2</sub> a promising green material has attracted considerable interests in virtue of its low cost, high environmental compatibility and wide structural diversity combined with unique physical and chemical properties [1-4]. Transition-metal oxides have been shown to be excellent electrode active materials due to their chemical stability, variable valence etc. Important applications of nano-sized MnO<sub>2</sub> include preparation of cathode materials of alkaline batteries [5], electrochemical capacitors [6], smart windows [7], the active layer for gas sensors [8] and photocatalyst [9]. In accomplishing the synthesis and manipulation of the nanostructured nickel oxide, a variety of strategies have been employed, such as evaporation [10], sputtering [11], electrodeposition [12], thermal decomposition [13] and sol-gel techniques [14]. Thermal decomposition method has some advantages such as simple process, low cost and easiness to obtain high purity products hence it is quite promising and facile route for industrial applications. Many reports have concerned the synthesis of NiO nanocrystals, including NiO nanorings [15], nanosheets [16], nanoribbons [17] and nanoclusters [18]. MnO<sub>2</sub> nanoparticles were synthesized by different methods including co-precipitation [19], microemulsion [20], sol-gel [21], sonochemical [22], hydrothermal [23] and electrochemical methods [24]. MnO<sub>2</sub> was the most unusual one in terms of its structural properties at ambient pressure, which are largely determined by the strong tendency for linear coordination of O-Mn-O chain geometry [25]. The structure of MnO<sub>2</sub> is built up of planar O-Mn-O zigzag chains lying in the ac-plane. The band gap of the MnO<sub>2</sub> structures at room temperature was measured to be 2.19 eV from the photoconductivity, and n-type electrical conductivity has been reported [26-28]. In this manuscript, the production method of MnO<sub>2</sub> nanostructures is reported. One-dimensional (1-D) nanostructures of MnO<sub>2</sub> nanocomposites were prepared by solid-state thermal decomposition of the as-produced Mn(CH<sub>3</sub>COO)<sub>2</sub> nanostructures. The utilized method has many advantages since it is a controllable, free solvent, template less, and economical method. The produced nanostructures were characterized by SEM, TEM, XRD, AFM, PL, and TGA.

## Experimental Section

### Materials and characterization

All the chemical reagents used in our experiments were of analytical grade and were used as received without further purification. X-ray diffraction (XRD) patterns were recorded by a Philips-X'Pert Pro, X-ray diffractometer using Ni-filtered Cu K $\alpha$  radiation at scan range of 10<2 $\theta$ <80 in Tehran university -IRAN. Scanning electron microscopy (SEM) images were obtained on LEO-1455VP equipped with an energy dispersive X-ray spectroscopy. Transmission electron microscope (TEM) images were obtained on a Philips EM208S transmission electron microscope with an accelerating voltage of 100 kV. Images were obtained on Electronic Nano Laboratory Technical University of Tehran-IRAN. Based on the information obtained Figure 1 from Taguchi method, Time, Temperature and surfactant all three cases showed a significant influence on the BET parameters, because the signal to noise (SN) varies with the level changes, all of parameter have influence on the size, pore diameter, pore volume and surface area parameter.

### Synthesis of Mn(OAc)<sub>2</sub> nanostructures

In this work, Manganese(II) acetate powders was used as the starting reagent. Mn(OAc)<sub>2</sub> as precursors was prepared in a vertical quartz pipe set in vacuum condition. Each experiment was carried out by loading 0.56 g of Manganese (II) acetate powder, then powder transferred to

\*Corresponding author: Sedyghe Akbari, Department of Chemistry, Kerman Branch, Islamic Azad University, Kerman, Iran, Tel: +98 559 5466467; E-mail: [Mohammadmehdi869@yahoo.com](mailto:Mohammadmehdi869@yahoo.com)

Received: December 28, 2017; Accepted: May 02, 2018; Published: May 08, 2018

Citation: Akbari S, Foroughi MM, Ranjbar M (2018) Solvent-free Synthesis and Characterization of MnO<sub>2</sub> Nanostructures and Investigation of Optical Properties. J Nanomed Nanotechnol 9: 498. doi: [10.4172/2157-7439.1000498](https://doi.org/10.4172/2157-7439.1000498)

Copyright: © 2018 Akbari S, et al. This is an open-access article distributed under the terms of the Creative Commons Attribution License, which permits unrestricted use, distribution, and reproduction in any medium, provided the original author and source are credited.

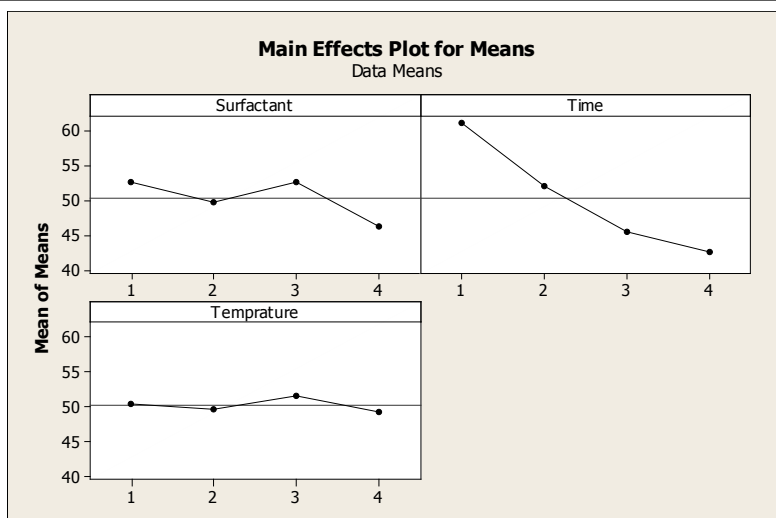


Figure 1: Data of surfactant, time and temperature on BET parameter with Taguchi technique.

Sample	Surfactant	Time (min)	Temperature	Size (nm)	BET		
					Pore diameter (Å)	Surface area (m <sup>2</sup> /g)	Pore volume (cm <sup>3</sup> /g)
1	SDS	60	200	54	10.6	1618	0.3741
2	CTAB	60	210	63	10.2	1864	0.3911
3	SDS	120	220	67	11.6	1927	0.4011
4	CTAB	120	230	66	12.2	2040	0.4030

Table 1: Reaction conditions for MnO<sub>2</sub> nanostructures.

the external pipe of the set. Then, the system was vacuumed by a pump. Water entered the inner pipe from one side and exited from the other side. Water was circulated in the system in order to solidify the product vapors. The sample was heated at 200°C for 120 min. After the heating process, the powder at the external part of the inner pipe was collected. The system was allowed to cool to room temperature naturally, and the obtained precipitations were collected. The as-synthesized powders were characterized by SEM.

### Synthesis of MnO<sub>2</sub> nanostructures

At first 0.5 g of the as-obtained Mn(OAc)<sub>2</sub> nanostructure was loaded into a silicon boat, then powders heated in air at 220°C, 240°C, 260°C for 120 min. After the heating process, the system was cool to room temperature naturally, and the obtained precipitation was collected. The as-synthesized powders were characterized and optimization by SEM, TEM, XRD, and PI (Table 1).

### Results and Discussion

In recent years, there has been major interest in the amplification of new compounds and the new method for the synthesis of materials [29]. Using the new method for preparation of nanomaterials can open new ways to control the shape and size distribution of nanostructures. In this work, Mn(OAc)<sub>2</sub> was applied as, manganese precursor due to its high thermal stability and less reactivity toward nucleophilic agents than other organometallic precursors. The XRD pattern of MnO<sub>2</sub> nanostructures obtained from solid-state thermal decomposition at 220°C is shown in Figure 2. All reflection peaks of the XRD pattern for MnO<sub>2</sub> nanoparticles are indexed well to orthorhombic phase with cell parameters corresponding to a=3.3110 Å and b=5.5260 Å. Based on XRD data, the crystallite diameter (D<sub>c</sub>) of MnO<sub>2</sub> nanoparticles can be

calculated using the Scherer equation [30]:

$$D_c = K\lambda / \beta \cos\theta \quad (\text{Scherer equation})$$

where β is the breadth of the observed diffraction line at its half intensity maximum, K is the so-called shape factor, which usually takes a value of about 0.9, and λ is the wavelength of X-ray source used in XRD. In the present research, the effect of the thermal decomposition temperature on the morphology of MnO<sub>2</sub> nanoparticles was investigated by SEM. SEM images of samples 1-3 were prepared at 220, 240 and 260°C, and called as samples a, b and c, respectively. Figure 3a-3c illustrates SEM images of the MnO<sub>2</sub> sublimated within the range of 220-260°C. The morphology of all samples is particle-like; however, by increasing the reaction temperature from 220 to 260°C, the particle size of the products increased. To further investigate the details of morphology, we took TEM image from the optimized sample. To prepare the TEM sample, first, the powder was dispersed in highly pure ethanol via ultrasonic equipment for 15 min. TEM image from the optimized sample of MnO<sub>2</sub> nanocomposite is shown in Figure 4. The MnO<sub>2</sub> nanocomposite consists of separated nanostructures that this image according to SEM image of samples, MnO<sub>2</sub> nanocomposites are separated structures. Due to the activation of the surface of nanoparticles, some areas have been cracked. Microscopic images confirm XRD pattern for MnO<sub>2</sub> nanoparticles.

Figure 5 shows an FT-IR spectrum of MnO<sub>2</sub> nanocomposites synthesized at 260°C for 120 min after thermal decomposition. As shown in Figure 5, the vibration peaks corresponding to the spinel structure are identified at about 567, 876 and 1011 cm<sup>-1</sup>. A weak peak centered at 1219 cm<sup>-1</sup> can be attributed to stretching vibration of the Mn-O band of MnO<sub>2</sub> and a strong peak centered at 3244 cm<sup>-1</sup> can be attributed to stretching vibration of the H-O band of H<sub>2</sub>O molecules

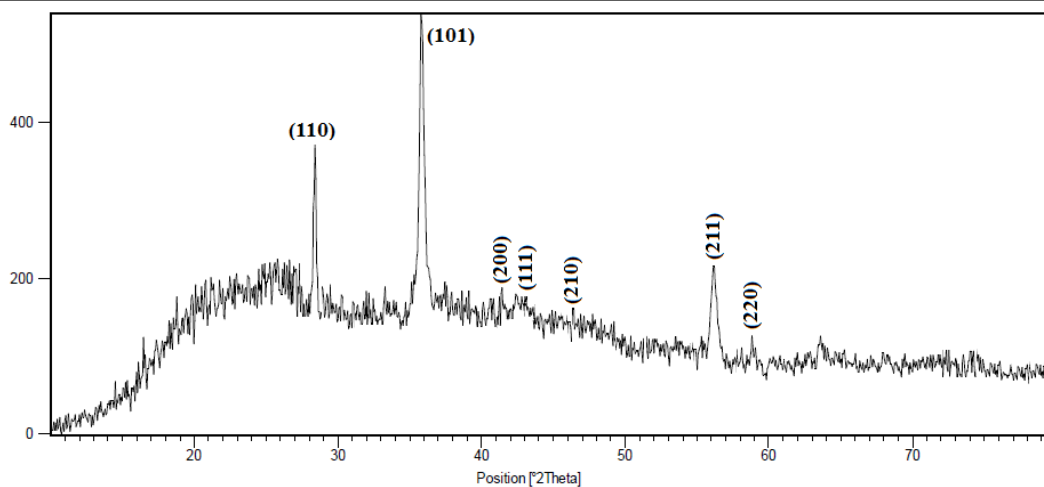


Figure 2: XRD patterns of MnO<sub>2</sub> nanostructures sublimated at 220°C for 120 min.

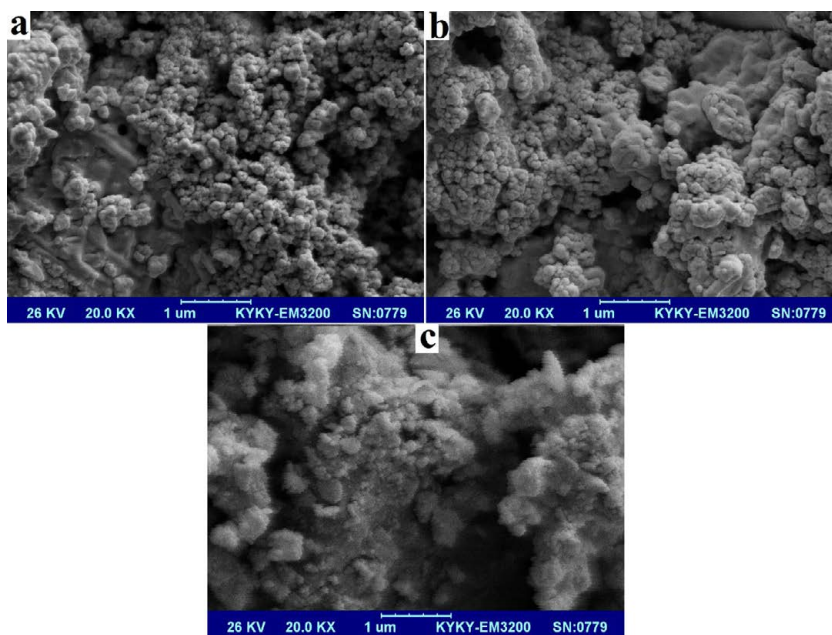


Figure 3: SEM images of the MnO<sub>2</sub> nanostructures sublimated at (a) 220 (b) 240 (c) 260°C.

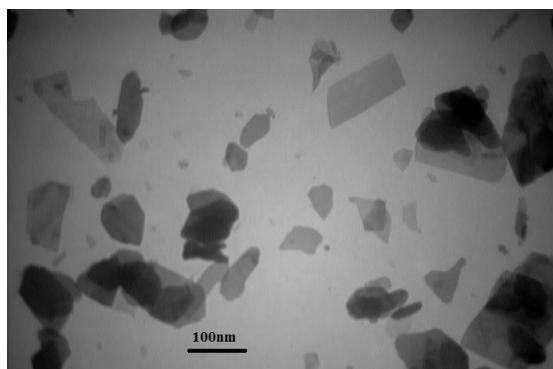


Figure 4: TEM image of the MnO<sub>2</sub> nanostructures synthesized sublimated at 220°C for 120 min.

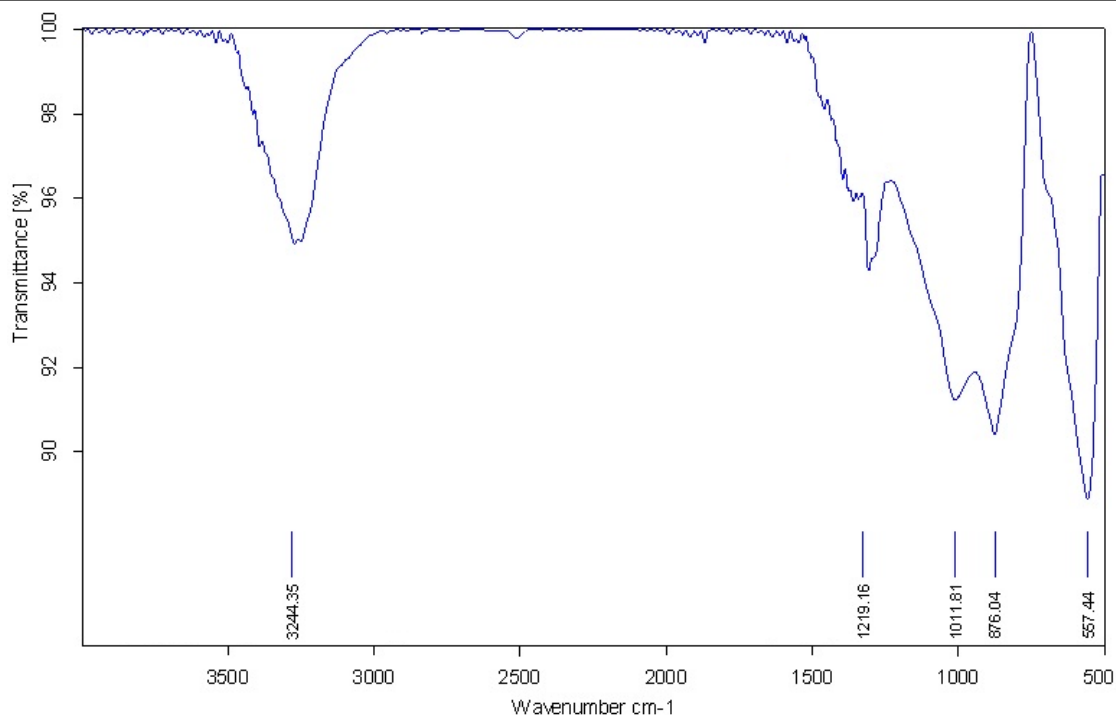


Figure 5: FT-IR spectrum of the MnO<sub>2</sub> nanostructures synthesized sublimated at 220°C for 120 min.

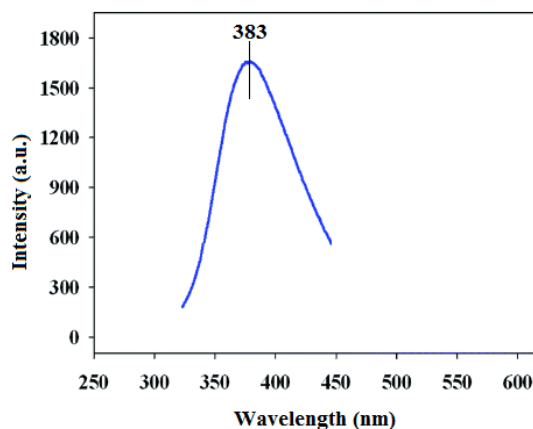


Figure 6: PL spectrum of MnO<sub>2</sub> nanostructures synthesized sublimated at 220°C for 120 min.

that was absorbed on the surface of the nanoparticle [30]. Room temperature PL spectrum of MnO<sub>2</sub> nanocomposites obtained from sample excited at 383 nm was presented in Figure 6, The emission spectrum shows a blue shift (2.6 eV, 460 nm), compared to that of the bulk MnO<sub>2</sub> nanocomposites. Such a large blue shift of excitonic absorption band can be attributed to the small crystallite size of the samples.

## Conclusions

In this work, MnO<sub>2</sub> nanostructures have been successfully synthesized through a solid-state thermal decomposition method. We investigated the influence of the thermal decomposition temperature on the morphology of MnO<sub>2</sub> nanostructures. The characteristics of products were determined by using XRD, SEM, TEM, IR and PL

analysis. The XRD results indicated that pure MnO<sub>2</sub> nanostructures without any impurities could be obtained after thermal decomposition at 200°C for 2 h. SEM images indicated that by increasing thermal decomposition temperature, distribution size of MnO<sub>2</sub> nanostructures increased and morphology of this structures are uniforms.

## References

1. Easton DF, Pharoah PD, Antoniou AC, Tischkowitz M, Tavtigian SV, et al. (2015) Gene-panel sequencing and the prediction of breast-cancer risk. *New England Journal of Medicine* 372: 2243-2257.
2. Martin AM, Weber BL (2000) Genetic and hormonal risk factors in breast cancer. *Journal of the National Cancer Institute* 92: 1126-1135.
3. Willett W (1989) The search for the causes of breast and colon cancer. *Nature* 338: 389-394.
4. Morales L, Alvarez-Garriga C, Matta J, Ortiz C, Vergne Y, et al. (2013) Factors

- associated with breast cancer in Puerto Rican women. *Journal of epidemiology and global health* 3: 205-215.
5. Liu YT, Gao CM, Ding JH, Li SP, Cao HX, et al. (2011) Physiological, reproductive factors and breast cancer risk in Jiangsu province of China. *Asian Pac J Cancer Prev* 12: 787-790.
  6. Diego EJ, McAuliffe PF, Soran A, McGuire KP, Johnson RR, et al. (2016) Axillary staging after neoadjuvant chemotherapy for breast cancer: a pilot study combining sentinel lymph node biopsy with radioactive seed localization of pre-treatment positive axillary lymph nodes. *Annals of surgical oncology* May 23: 1549-1553.
  7. Swain SM, Ewer MS, Viale G, Delalage S, Ferrero JM, et al. (2017) Abstract P4-21-41: Primary analysis of BERENICE: A phase II cardiac safety study of pertuzumab, trastuzumab, and neoadjuvant anthracycline-based chemotherapy in patients with locally advanced, inflammatory, or early-stage, unilateral, and invasive HER2-positive breast cancer. *Cancer Research* 77: 21-41.
  8. Burstein HJ, Temin S, Anderson H, Buchholz TA, Davidson NE, et al. (2014) Adjuvant endocrine therapy for women with hormone receptor-positive breast cancer: American Society of Clinical Oncology clinical practice guideline focused update. *Journal of Clinical Oncology* 32: 2255-2269.
  9. Drăgănescu M, Carmocan C (2017) Hormone Therapy in Breast Cancer. *Chirurgia* 112: 413-417.
  10. den Hollander P, Savage MI, Brown PH (2013) Targeted therapy for breast cancer prevention. *Front Oncol* 3: 250.
  11. Janni W (2016) Targeted Therapy of Breast Cancer. *Oncology research and treatment* 39: 100-101.
  12. Coates A, Abraham S, Kaye SB, Sowerbutts T, Frewin C, et al. (1983) On the receiving end-patient perception of the side-effects of cancer chemotherapy. *Eur J Cancer Clin Oncol* 19: 203-208.
  13. Grem JL (2000) 5-Fluorouracil: forty-plus and still ticking: A review of its preclinical and clinical development. *Investigational New Drugs* 18: 299-313.
  14. Noordhuis P, Holwerda U, Van der Wilt CL, Van Groeningen CJ, Smid K, et al. (2004) 5-Fluorouracil incorporation into RNA and DNA in relation to thymidylate synthase inhibition of human colorectal cancers. *Ann Oncol* 15: 1025-1032.
  15. Cohen SS, Flaks JG, Barner HD, Loeb MR, Lichtenstein J (1958) the mode of action of 5-fluorouracil and its derivatives. *Proc Natl Acad Sci USA* 44: 1004-1012.
  16. Eskandari MR, Moghaddam F, Shahraki J, Pourahmad J (2015) A comparison of cardiomyocyte cytotoxic mechanisms for 5-fluorouracil and its pro-drug capecitabine. *Xenobiotica* 45: 79-87.
  17. Arias JL (2008) Novel strategies to improve the anticancer action of 5-fluorouracil by using drug delivery systems. *Molecules* 13: 2340-2369.
  18. Boisdron-celle M, Menei PH, Benoit JP (1995) Preparation and Characterization of 5-Fluorouracil-loaded Microparticles as Biodegradable Anticancer Drug Carriers. *J Pharm Pharmacol* 47: 108-114.
  19. Denizli A, Kiremitci M, Pişkin E (1989) Subcutaneous polymeric matrix system p (HEMA-BGA) for controlled release of an anticancer drug (5-fluorouracil): II: Release kinetics. *Biomaterials* 9: 363-366.
  20. Zhuo RX, Du B, Lu ZR (1999) In vitro release of 5-fluorouracil with cyclic core dendritic polymer. *J Control Release* 57: 249-257.
  21. Sato S, Itamochi H, Kigawa J, Oishi T, Shimada M, et al. (2009) Combination chemotherapy of oxaliplatin and 5-fluorouracil may be an effective regimen for mucinous adenocarcinoma of the ovary: a potential treatment strategy. *Cancer Sci* 100: 546-551.
  22. Chandran SP, Natarajan SB, Chandraseharan S, Shahimi MS (2017) Nano drug delivery strategy of 5-fluorouracil for the treatment of colorectal cancer. *Journal of Cancer Research and Practice* 4: 45-48.
  23. Bassiouni Y, Faddah L (2012) Nanocarrier-Based Drugs: The Future Promise for Treatment of Breast Cancer. *Journal of Applied Pharmaceutical Science* 2: 225-232.
  24. Bagalkot V, Zhang L, Levy-Nissenbaum E, Jon S, Kantoff PW, et al. (2007) Quantum dot-aptamer conjugates for synchronous cancer imaging, therapy, and sensing of drug delivery based on bi-fluorescence resonance energy transfer. *Nano Lett* 7: 3065-3070.
  25. He C, Lu K, Liu D, Lin W (2014) Nanoscale metal-organic frameworks for the co-delivery of cisplatin and pooled siRNAs to enhance therapeutic efficacy in drug-resistant ovarian cancer cells. *J Am Chem Soc* 136: 5181-5184.
  26. Pan L, He Q, Liu J, Chen Y, Ma M, et al. (2012) Nuclear-targeted drug delivery of TAT peptide-conjugated monodisperse mesoporous silica nanoparticles. *J Am Chem Soc* 134: 5722-5725.
  27. Rasmussen JW, Martinez E, Louka P, Wingett DG (2010) Zinc oxide nanoparticles for selective destruction of tumor cells and potential for drug delivery applications. *Expert Opin Drug Deliv* 7: 1063-1077.
  28. Shi J, Votruba AR, Farokhzad OC, Langer R (2010) Nanotechnology in drug delivery and tissue engineering: from discovery to applications. *Nano Lett* 10: 3223-3230.
  29. Aydin R, Pulat M (2012) 5-Fluorouracil encapsulated chitosan nanoparticles for pH-stimulated drug delivery: evaluation of controlled release kinetics. *Journal of Nanomaterials*.
  30. Sirelkhatim A, Mahmud S, Seeni A, Kaus NH, Ann LC, et al. (2015) Review on zinc oxide nanoparticles: antibacterial activity and toxicity mechanism. *Nano-Micro Letters* 7: 219-242.